

Transient Response of the Southern Ocean to Changing Ozone: Regional Responses and Physical Mechanisms

WILLIAM J. M. SEVIOUR, ANAND GNANADESIKAN, DARRYN WAUGH, AND MARIE-AUDE PRADAL

Department of Earth and Planetary Sciences, Johns Hopkins University, Baltimore, Maryland

(Manuscript received 27 June 2016, in final form 22 November 2016)

ABSTRACT

The impact of changing ozone on the climate of the Southern Ocean is evaluated using an ensemble of coupled climate model simulations. By imposing a step change from 1860 to 2000 conditions, response functions associated with this change are estimated. The physical processes that drive this response are different across time periods and locations, as is the sign of the response itself. Initial cooling in the Pacific sector is driven not only by the increased winds pushing cold water northward, but also by the southward shift of storms associated with the jet stream. This shift drives both an increase in cloudiness (resulting in less absorption of solar radiation) and an increase in net freshwater flux to the ocean (resulting in a decrease in surface salinity that cuts off mixing of warm water from below). A subsurface increase in temperature associated with this reduction in mixing then upwells along the Antarctic coast, producing a subsequent warming. Similar changes in convective activity occur in the Weddell Sea but are offset in time. Changes in sea ice concentration also play a role in modulating solar heating of the ocean near the continent. The time scale for the initial cooling is much longer than that seen in NCAR CCSM3.5, possibly reflecting differences in natural convective variability between that model (which has essentially no Southern Ocean deep convection) and the one used here (which has a large and possibly unrealistically regular mode of convection) or to differences in cloud feedbacks or in the location of the anomalous winds.

1. Introduction

Does the ozone hole warm or cool the Southern Ocean? Recent work has suggested that the answer may depend on the time scale involved. In a simulation with the Massachusetts Institute of Technology (MIT) idealized coupled climate model MITgcm, [Ferreira et al. \(2015, hereafter F15\)](#) found that the initial response to the creation of an instantaneous ozone hole was to cool the surface. They argued that an increase in Southern Ocean westerlies resulted in an Ekman flow that pushed cold water northward, a response lasting for about 10 years. Following this, a warming was generated as warmer subsurface waters were brought to the surface, entrained into the mixed layer, and advected northward. [F15](#) suggested that this response could explain why recent trends in Antarctic sea ice extent ([Simmonds 2015; Parkinson and diGirolamo 2016](#)) show an increase but suggest that this increase might reverse in the future. [Armour et al. \(2016\)](#) also show that the advection of

unmodified warm deep waters to the surface plays an important role in delaying the onset of global warming, although in their paper it is a change in the temperature gradient along the path of flow rather than a change in the amount of flow that causes a relative cooling.

However, when [F15](#) simulated the impact of an ozone hole in the NCAR CCSM3.5 model, the results were very different than in MITgcm. In CCSM3.5, the cooling lasted for a much shorter duration and the warming came to equilibrium within about five years. The NCAR CCSM3.5 has a much more realistic ocean bathymetry. Given the vital role of form drag in the dynamics of the Antarctic ([Gille 1997](#)) one might expect a more realistic bathymetry to produce a different partitioning of overturning and eddy response ([Hallberg and Gnanadesikan 2001](#)) than an idealized one. CCSM3.5 also has a more sophisticated treatment of atmospheric processes such as clouds than the version of MITgcm in [F15](#), allowing for tradeoffs between penetrative deep convection and stratiform convection. If more realistic models always predicted a short cooling and quick warming in response to the ozone hole, ozone would be unlikely to explain the recent cooling. Instead, it would be more likely that

Corresponding author e-mail: Anand Gnanadesikan, gnanades@jhu.edu

the cooling and expansion of sea ice was due to natural variability (Turner et al. 2016).

However, as noted by de Lavergne et al. (2014) the NCAR model series may be somewhat of an outlier in terms of natural variability. Many models simulate quasi-periodic deep convection in the Southern Ocean (Galbraith et al. 2011, hereafter GEA11; Martin et al. 2013) and the cessation of this convection associated with global warming may result in a localized cooling. Given that the NCAR model series has essentially no convective variability, it seemed useful to us to examine a model with realistic geometry and cloud physics in which convection is strong and relatively regular. In a companion paper (Seviour et al. 2016, hereafter SEA1), we examined the response of the GFDL ESM2Mc model (GEA11) to a step change from preindustrial to modern ozone concentrations. This model has relatively strong convective variability (GEA11; de Lavergne et al. 2014). As discussed in Latif et al. (2013) there is some evidence for such variability, although it is only based on a few proxy records. Unfortunately the satellite record is short and, if de Lavergne et al. (2014) are correct, it may only capture the recent cessation of convective activity. Our study should therefore be considered an exploration of how a highly convective model behaves in the presence of an ozone hole.

In SEA1 we showed that convective variability could complicate detecting ozone-driven changes as it is larger than the signal associated with ozone and may modulate the response to changing ozone. SEA1 also showed that the behavior of the response differed between the Ross and Weddell Seas but did not explain why this difference occurred. Additionally, SEA1 examined the sensitivity of ozone-driven changes to details in how the ozone hole is represented by forcing the model with monthly-mean and daily-mean ozone concentrations. Because the ozone hole is relatively short-lived, forcing with daily concentrations better resolves the seasonal minimum in ozone concentrations, producing more cooling and a significantly stronger wind response. Based on the results of F15 we would expect a larger temperature response and shorter time scale for cooling (as the rates of both advection and entrainment would be expected to increase). However, the SST response for the two cases was essentially identical both spatially and temporally.

In this paper we examine this regional response in more detail and focus on the actual mechanisms that cause changes in temperature. We demonstrate that different processes dominate in different regions and at different times. Our model differs from those reported in F15 in several ways. First, the vertical mixing of heat from below plays an important role in explaining the pattern of the initial cooling. This change in mixing is mediated by changes in the upper ocean stability

associated with shifts in the hydrological cycle. Second, while the latent, sensible, and longwave heat fluxes act to damp the temperature anomalies, in our model changes in solar heating of the surface ocean can act to reinforce them. This contrasts with CCSM3.5 (where the shortwave fluxes damp the initial cooling) and MITgcm (where they are essentially neutral), suggesting that the details of cloud response may also be important.

2. Methods

a. Model description

We begin by quickly summarizing the model and experimental strategy used here. The physical model is the GFDL ESM2Mc model, described in more detail in GEA11. This model has an atmospheric resolution of 3.875° in the east–west direction, 3° in the north–south direction, and 24 layers in the vertical. The ocean model resolution is 3° in the east–west direction and varies from 2° to $2/3^\circ$ in the north–south direction, with finer resolution in the tropics and Southern Ocean. The models contain up-to-date physical parameterizations of a wide variety of processes, including atmospheric convection due to stratus, shallow cumulus, and cumulonimbus and diurnally varying atmospheric radiation (Delworth et al. 2006; GEA11). The results presented here all use 1860 values for solar insolation and all greenhouse gases other than ozone, which is also held at 1860 values in the control simulation. Three-dimensional distributions of multiple aerosols including sulfate, black carbon, and eight size classes of mineral dust are fixed at 1860 levels as well. The model has a good representation of El Niño–Southern Oscillation (ENSO; Russell and Gnanadesikan 2014) and the southern annular mode (GEA11), two important features of variability with relevance for the Southern Ocean. Southern Hemisphere sea ice has a minimum seasonal extent of 0.10 million km^2 (Mkm^2) and a maximum seasonal extent of 14.5 Mkm^2 . Both of these are smaller than the observed values of 3.0 and 18.4 Mkm^2 with an RMS error of 4.7 Mkm^2 . During nonconvective time periods, however, the maximum ice extent rises to 16.4 Mkm^2 while the minimum remains essentially unchanged. The RMSE during nonconvective periods drops to 3.7 Mkm^2 , putting ESM2Mc in the middle of the 18 CMIP5 models described in Turner et al. (2013). CCSM3.5, by contrast, has a very attenuated seasonal cycle of sea ice (Bitz and Polvani 2012) with far too much sea ice ($\sim 7.5 \text{Mkm}^2$) during the summer months. Later versions of the model, such as the CESM1 studied in de Lavergne et al. (2014), have even more extreme high biases (Turner et al. 2013).

The original series of ESM2Mc models used the default ozone field distributed with the CM2 model

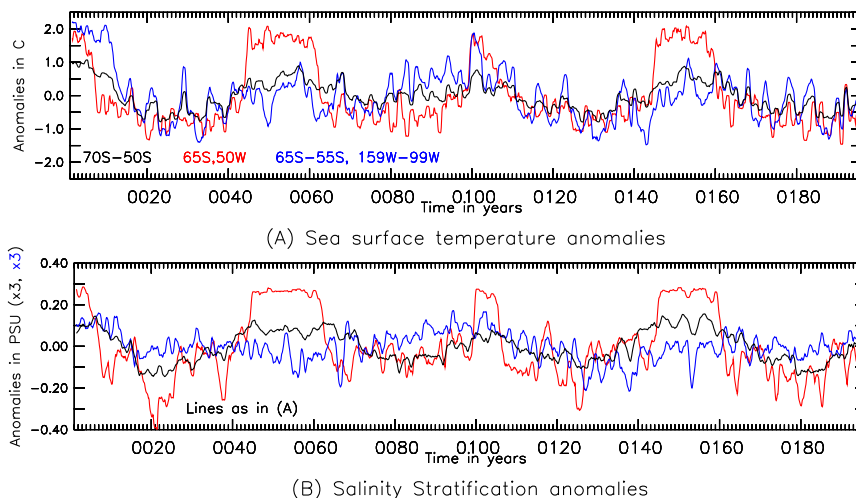


FIG. 1. Relationship between interannual variability in SST and salinity stratification in GFDL ESM2Mc model. (a) SST anomalies over the entire Southern Ocean between latitudes of 70° and 50°S (black line), at a single point (65°S, 50°W) in the Weddell Sea (red line) and averaged over 65°–55°S, 159°–99°W (Pacific sector of the Southern Ocean). (b) As in (a), but showing the difference between surface salinity and salinity at level 10 (120 m). Values for the Southern Ocean as a whole and the Pacific sector are scaled up by a factor of 3.

series. This field improperly mapped the ozone in the vertical with far too much ozone in the topmost model levels. The present model series uses the SPARC 1860 distribution (Cionni et al. 2011) as a control and thus has a baseline that is slightly warmer and less stratified in the Southern Ocean than the versions reported in GEA11 and Pradal and Gnanadesikan (2014). The jet in our version of ESM2Mc is slightly shifted equatorward with a peak at 49.5°S.

As discussed in a number of papers (GEA11; Pradal and Gnanadesikan 2014; de Lavergne et al. 2014; SEA1) the ESM2Mc models exhibit significant convective variability in the Southern Ocean. The stabilizing stratification in the Southern Ocean is primarily due to salinity and GEA11 found that salinity anomalies in the eastern Weddell Sea offered some predictability of when convection would turn on or off. Pradal and Gnanadesikan (2014) showed that on an annual basis the correlation between sea surface temperatures and the salinity difference between 200 m and the surface exceeded 0.9 in many parts of the Southern Ocean. Figure 1 illustrates this result, showing time series of both the SST anomaly and the salinity difference at two points, one in the middle of the Weddell Sea at 65°S, 50°W (the center of the convection studied by GEA11) and the other in the Pacific at 65°–55°S, 159°–99°W [the region of the convection studied by Pradal and Gnanadesikan (2014)], as well as averages between 50° and 70°S over 200 years of the control used in this experiment. The Weddell Sea (red lines) shows a series of sharp rises and falls in

temperature, with peak warm anomalies reaching up to 2°C (Fig. 1a). The Pacific sector (blue lines) shows both high- and low-frequency variability. The pan-Southern Ocean temperatures clearly respond to the two convective sites, with some tendency to exhibit peaks near the end of a convective period. The salinity stratification (Fig. 1b) varies together with the temperature. This is most clearly seen at 65°S, 50°W (red lines), where the correlation coefficient between salinity stratification and SST is 0.87. For the Southern Ocean as a whole the correlation is 0.76 for annually averaged salinity and SST, and 0.86 when a decadal average is taken. For the Pacific sector section the correlation is less clear, but is still a relatively high 0.44 when annual smoothing is done and 0.77 when both fields are decadal smoothed. We note that the time series in the Weddell Sea and Pacific sector have different characters, with the former showing a “top hat” shape and the later more gentle, long-term variability. This reflects a fundamental difference in the character of the convection in the two locations. The Weddell Sea sees deep convection analogous to the Weddell polynya, while in the Pacific sector the variability reflects different degrees of penetration into the warm, salty waters of the upper pycnocline.

b. Retrieving a response function

A number of investigators (Branstator 1985; Menemenlis et al. 2005; F15; Gnanadesikan et al. 2015; Marshall et al. 2015) have considered the possibility of using response

functions in which finite-amplitude changes are applied to the climate system instantaneously and the resulting evolution is then computed over time in order to characterize the fundamental dynamics of the system. In coupled climate models it is necessary to smooth out the effects of natural variability. To do this, multiple simulations are started at different times and the solution is then ensemble-averaged. This allows averaging over the response due to processes such as ENSO, which are decorrelated at the model start times.

However, the presence of long-period variability introduces a number of complications to how these initial start times are chosen. If the variability is large in comparison with the response, transient responses that start in a warm phase will tend to show cooling, while those that start in a cold phase will tend to show warming. As discussed in [SEA1](#), we addressed this by running 24 perturbation experiments for 48 years each. We take 12 initial start times distributed between 6 warm (centered at years 55 and 155) and 6 cold periods (centered at years 30 and 130). For each start, two perturbation runs were started, one in which monthly ozone concentrations from the year 1860 were replaced with monthly ozone concentrations from the year 2000 and the other in which they were replaced with daily ozone concentrations from the year 2000. Ensemble averages were then created for those runs using daily forcing, for those runs using monthly forcing, and for both sets of runs. Systematic differences between the two ozone forcings are seen in the wind response, which is about 20% weaker across the latitudes of Drake Passage, in the model forced by monthly ozone (see Fig. 3a in [SEA1](#)). This is because using monthly ozone tends to smooth away the peak depletion. However, as discussed in [SEA1](#), virtually no difference is seen between the ensemble-averaged daily and monthly SST responses. The small differences in the radiative forcing do result in differences in atmospheric convection, which cause the weather and interannual variability within the daily and monthly ozone simulations to diverge rapidly. Unless we specifically indicate otherwise, we will examine the difference between the ensemble average of all 24 perturbation runs and a 100-yr control climatology. As discussed in [SEA1](#) the initial ensemble is slightly colder than the control, but this perturbation would be expected to decay over the first decade, rather than amplifying and persisting as it does in the ensemble with perturbed ozone.

c. Model term balances

To understand the evolution of the ocean temperature at each point the time tendency is broken up into the following terms:

$$\begin{aligned} \left(\frac{\partial T'}{\partial t}\right)_{\text{total}} = & \left(\frac{\partial T'}{\partial t}\right)_{\text{advect}} + \left(\frac{\partial T'}{\partial t}\right)_{\text{neutral}} + \left(\frac{\partial T'}{\partial t}\right)_{\text{submeso}} \\ & + \left(\frac{\partial T'}{\partial t}\right)_{\text{vdiff}} + \left(\frac{\partial T'}{\partial t}\right)_{\text{nonlocalKPP}} + \left(\frac{\partial T'}{\partial t}\right)_{\text{SWpen}}, \end{aligned} \quad (1)$$

where T' represents the perturbation temperature. The left-hand side refers to the total heating/cooling (essentially zero over a century but potentially significant on shorter times scales). The first term on the right-hand side is the tendency due to the resolved advection within the model in all three dimensions. The second term on the right-hand side includes the parameterized effect of mesoscale eddies from both the Gent and McWilliams (advective) and Redi diffusion (along-isopycnal mixing) terms ([Gent and McWilliams 1990](#); [Griffies et al. 1998](#)). The third term is submesoscale mixing following [Fox-Kemper et al. \(2011\)](#). Vertical mixing in the model follows the basic pattern suggested by [Troen and Mahrt \(1986\)](#) for the atmospheric boundary layer in which the vertical heat tendency is

$$\frac{\partial T}{\partial t} = \frac{\partial}{\partial z} K_v \left(\frac{\partial T}{\partial z} - \gamma \right), \quad (2)$$

where K_v is a vertically varying mixing coefficient and $\gamma(z)$ parameterizes a ‘‘countergradient’’ term that allows for transport by large eddies that feel the large-scale gradient across the boundary layer rather than the local gradient (which may have the opposite sign). The fourth term in Eq. (1) (with the subscript ‘‘vdiff’’) is associated with turbulent (downgradient) diffusion associated with the first of the terms within the parentheses in Eq. (2). The fifth term (with the subscript ‘‘nonlocalKPP’’) represents the countergradient term following the K profile parameterization (KPP) of [Large et al. \(1994\)](#), which generally produces the largest effect at the base of the mixed layer. The final term is a source term from penetrating shortwave radiation that removes heat deposited in the surface layer and redistributes it through the water column. In general we will combine the two subgrid-scale eddy parameterization terms that depend on the 3D density structure to get a parameterized eddy tendency

$$\left(\frac{\partial T'}{\partial t}\right)_{\text{eddy}} = \left(\frac{\partial T'}{\partial t}\right)_{\text{neutral}} + \left(\frac{\partial T'}{\partial t}\right)_{\text{submeso}}, \quad (3)$$

and the last three terms to get

$$\left(\frac{\partial T'}{\partial t}\right)_{\text{vmix}} = \left(\frac{\partial T'}{\partial t}\right)_{\text{vdiff}} + \left(\frac{\partial T'}{\partial t}\right)_{\text{nonlocalKPP}} + \left(\frac{\partial T'}{\partial t}\right)_{\text{SWpen}}. \quad (4)$$

Including the shortwave penetration in this term is useful, since much of the signal within the mixed layer is simply to smooth out the resulting heterogeneous deposition of energy. We can also get significant insight by summing some of these terms in the vertical. For example, when the vertical diffusion term is vertically summed over the entire water column, the result is to get the sum of the fluxes into the ocean at both the surface and the bottom:

$$\sum_{k=1}^{28} \left[\rho_k c_p \left(\frac{\partial T}{\partial t} \right)_{\text{vdiff}} \right]_k \delta z_k = Q_{\text{SW}} + Q_{\text{lw}} + Q_{\text{lat}} + Q_{\text{sens}} + Q_{\text{geo}} = Q_{\text{surf}} + Q_{\text{geo}}, \quad (5)$$

where c_p is the specific heat, ρ_k , δz_k are the density and thickness of box k , and the terms on the right-hand side refer to the net shortwave radiative flux at the ocean surface, the net longwave radiative flux, the net flux from any state change of water (evaporation, melting/freezing of sea ice, melting of snow), net sensible heat fluxes, and geothermal heating at the ocean bottom, respectively. The term Q_{geo} is identical in the control and ozone perturbation cases. By taking the difference between these sums, we can thus isolate the difference in surface fluxes, and by subtracting the difference in Q_{SW} we can focus on the fluxes that are due to exchanges at the top of the ocean. We will refer to this difference as

$$\Delta Q_{\text{non-solar}} = \Delta Q_{\text{surf}} - \Delta Q_{\text{SW}} = \Delta Q_{\text{lw}} + \Delta Q_{\text{lat}} + \Delta Q_{\text{sens}}. \quad (6)$$

Similarly, because $(\partial T/\partial t)_{\text{nonlocalKPP}}$ and $(\partial T/\partial t)_{\text{vdiff}}$ represent flux divergences that either vanish or are unchanging on the bottom boundary, we can sum from the bottom of the ocean to a box with a bottom at 60 m to find the changes in fluxes through a nominal depth of 60 m:

$$\Delta Q_{\text{vmix}}(60 \text{ m}) = \sum_{k=6}^{28} \Delta \left[\rho_k c_p \left(\frac{\partial T}{\partial t} \right)_{\text{vmix}} \right]_k \delta z_k, \quad (7a)$$

$$\Delta Q_{\text{nonlocalKPP}}(60 \text{ m}) = \sum_{k=6}^{28} \Delta \left[\rho_k c_p \left(\frac{\partial T}{\partial t} \right)_{\text{nonlocalKPP}} \right]_k \delta z_k. \quad (7b)$$

Similarly $(\partial T/\partial t)_{\text{eddy}}$ and $(\partial T/\partial t)_{\text{adv}}$ are summed over the top 60 m to give the heat flux into a 1 m^2 column associated with the 3D fluxes, allowing us to compute

$$\Delta Q_{\text{adv}}(0 - 60 \text{ m}) = \sum_{k=1}^5 \Delta \left[\rho_k c_p \left(\frac{\partial T}{\partial t} \right)_{\text{adv}} \right]_k \delta z_k, \quad (8a)$$

$$\Delta Q_{\text{eddy}}(0 - 60 \text{ m}) = \sum_{k=1}^5 \Delta \left[\rho_k c_p \left(\frac{\partial T}{\partial t} \right)_{\text{eddy}} \right]_k \delta z_k. \quad (8b)$$

We analyze the importance of different mechanisms in producing temperature changes by generalizing the analysis of climate forcing and climate sensitivity often used to understand global warming to look at spatial patterns of temperature change. Without loss of generality, we can write the heat budget for a layer of depth H as

$$\rho c_p H \frac{\partial T}{\partial t} = Q + \lambda T', \quad (9)$$

where the time tendency term on the left-hand side represents a change in heat content, Q a heat flux, and λ the ‘‘sensitivity’’ of the system. If the first term associated with heat storage were small (a point to which we will return later) and λ were uniform (which in the presence of varying wind fields will only be approximately true), we could write the temperature anomaly as

$$T' \approx -Q/\lambda. \quad (10)$$

Insofar as this picture is correct, we would expect to see spatial correlation between changes in the supply of heat to the mixed layer and the resulting temperature change. Similarly, we can define sensitivity coefficients for different fluxes by looking for the part of the changes in nonsolar air–sea flux, 3D advective heat flux, vertical diffusive flux of heat from below, eddy heating, and the solar flux, that can be described respectively as $\lambda_{\text{nonsolar}} T'$, $\lambda_{\text{adv}} T'$, $\lambda_{\text{vmix}} T'$, $\lambda_{\text{eddy}} T'$, and $\lambda_{\text{SW}} T'$. The different λ terms represent spatial regression coefficients. We can also look at the regression coefficient of the total temperature tendency on temperature anomaly, which we will call λ_{tend} . The relative sizes of the λ terms help us to pick out which terms are most important in setting the spatial structure of the temperature anomaly. Positive correlations and regression coefficients suggest that the particular terms involved reinforce the anomaly pattern, while negative correlations and regression coefficients suggest that those terms damp the anomaly pattern. The analysis will only work if the patterns evolve on time scales comparable to the decadal averaging period; otherwise, the time-dependent terms will be important.

3. Results

a. Wind changes

It is by no means clear that all changes in winds over the Southern Hemisphere in recent years are due to ozone, especially with carbon dioxide and natural variability playing potentially important roles (Thomas et al. 2015). Nonetheless, within ESM2Mc the change in zonal mean

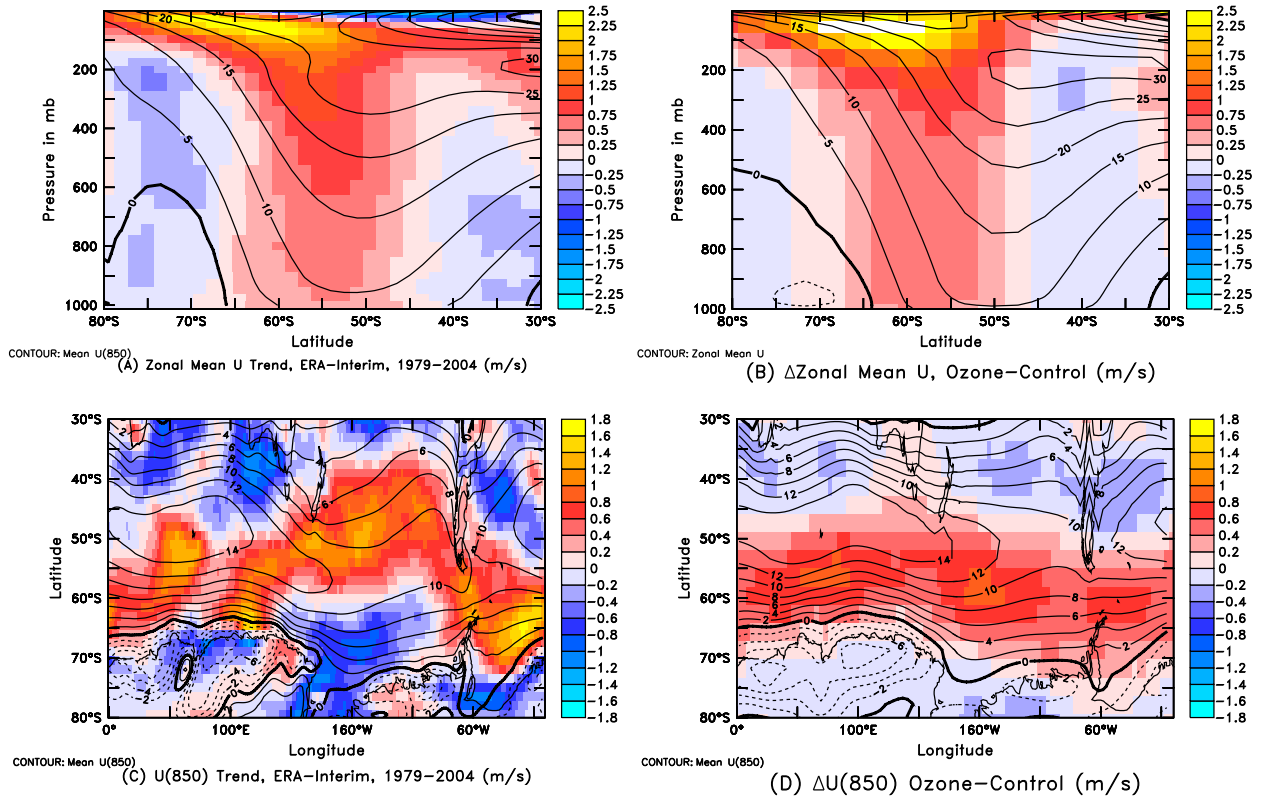


FIG. 2. Southern Ocean winds in observations and ESM2Mc. (a) Colors show 1979–2004 zonal mean trend in winds from the ERA-Interim reanalysis. Linear trend is computed and then applied over 25-yr period, following Thomas et al. (2015). Contours show mean wind over the time period. (b) Colors show difference between ESM2Mc run with ozone depletion during first decade and control. Contours show mean wind (average between ozone depletion and control so as to be consistent with observations during a time of change). (c),(d) As in (a),(b) but for winds at 850 mb.

winds (colors, Fig. 2b) maps well onto the observed trends in winds from 1979 to 2004 in the ERA-Interim reanalysis (Dee et al. 2011; colors, Fig. 2a) with peak increases exceeding 2 m s^{-1} above 200 mb between 70° and 60°S and downward propagation of this signal into the lower atmosphere, although with a signal that is slightly too broad and shifted a little poleward. In ERA-Interim the mean jet location is at around 51°S , with the peak of the increase in winds located only a few degrees south of that, so that the mean response is both an intensification and a broadening of the jet. With a peak increase in the jet located around 55°S , ESM2Mc captures this qualitative pattern with relatively realistic increases in wind speed. By contrast CCSM3.5 puts the initial jet slightly poleward of the true location, but the wind stress perturbation due to ozone peaks at a latitude of 62°S , far to the south of what is observed, and has little change at the latitude of the mean jet (Fig. 1 in F15). MITgcm has the change in wind stress in about the right place, but it locates the mean jet at about 43°S and again shows more of a shift than an intensification (also Fig. 1 in F15). Despite having relatively large changes in winds, ESM2Mc

has a smaller change in maximum wind stress than in the ERA-Interim reanalysis and a far smaller change than in the NCEP–NCAR reanalyses. Thomas et al. (2015) found a similarly large underestimate of the change in surface stress in all the CMIP5 models analyzed therein, suggesting either some bias in the reanalysis or some common deficiency in vertical momentum transport within the models.

Following Thomas et al. (2015) we now turn to the winds at 850 mb, where changes are more consistent across reanalyses than are surface stresses. Here we see some differences between the mean wind and its response to ozone in the ERA-Interim reanalysis (Fig. 2c) and ESM2Mc (Fig. 2d). ESM2Mc correctly captures the maximum in winds seen in the Indian Ocean sector as well as the wavy structure of the jet through this region. However, it does not capture the northward swerve of the jet over the southeast Pacific. In the ERA-Interim reanalysis, the 1979–2004 trend in winds reveals a southward shift of the winds over the Indian and Atlantic sectors of the Southern Ocean but an intensification and broadening over the Pacific sector.

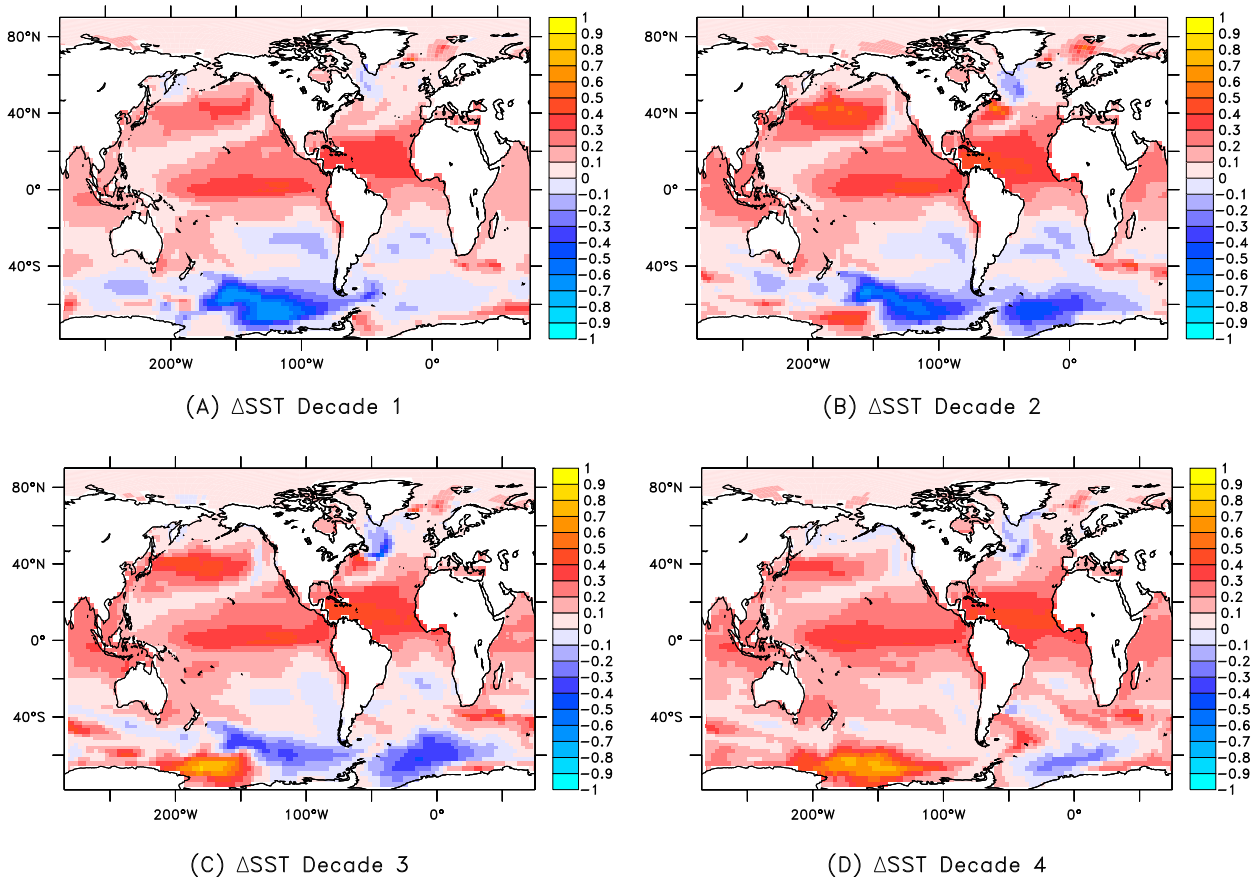


FIG. 3. SST anomalies (in K) in ensemble-mean ozone run compared with control for four consecutive decades, illustrating how the anomalies modulate convection in the Ross and Weddell Seas.

ESM2Mc shows more of a shift throughout the domain. Taken together, however, the model is consistent with ozone playing a predominant role in explaining the observed changes in winds.

b. Spatial structure of upper ocean temperature budget

Decadal snapshots of the temperature anomaly associated with changing ozone from 1860 to 2000 values (Fig. 3) show a quite striking pattern. In the first decade, a cooling of up to 0.7 K is seen in the Pacific sector centered around 60°S, 150°W, overlapping strongly with the convective region discussed in Pradal and Gnanadesikan (2014). This cooling weakens in the second and third decades of the perturbation, while a second cooling develops in the Weddell Sea, centered to the east of the region of deep convection. Simultaneously, a warming signal appears along the continent in the western Ross Sea. In the fourth decade this warming expands in the Pacific, but cooling persists in the Weddell Sea. Over the following eight years this cooling actually intensifies (SEA1, their Fig. 10). Additionally, we see an initial

warming at low latitudes with the Earth as a whole warming by around 0.16 K by the final decade. This is consistent with an initial decrease in outgoing longwave radiation of $\sim 0.4 \text{ W m}^{-2}$ due to tropospheric ozone (Ramaswamy et al. 2001).

What terms are responsible for producing this pattern of change in the Southern Ocean? We begin by evaluating the relationships between the fluxes into the top 60 m and the temperature anomalies over this depth range. In Fig. 4 we look at the relationship between the temperature anomaly and fluxes over the first decade, computing correlation and regression coefficients for the region south of 30°S. In Fig. 5 we plot these coefficients (computed using decadal smoothed anomalies and fluxes) over the whole experiment.

We would expect a strong relationship between $\Delta Q_{\text{non-solar}}$ (colors in Fig. 4a) and T' , as warmer temperatures would be expected to be associated with more longwave radiation to space, increased evaporation, and increased sensible heat loss to the atmosphere. Contours of the decadal SST anomaly (contours overlaid in Fig. 4a) show that during the first decade,

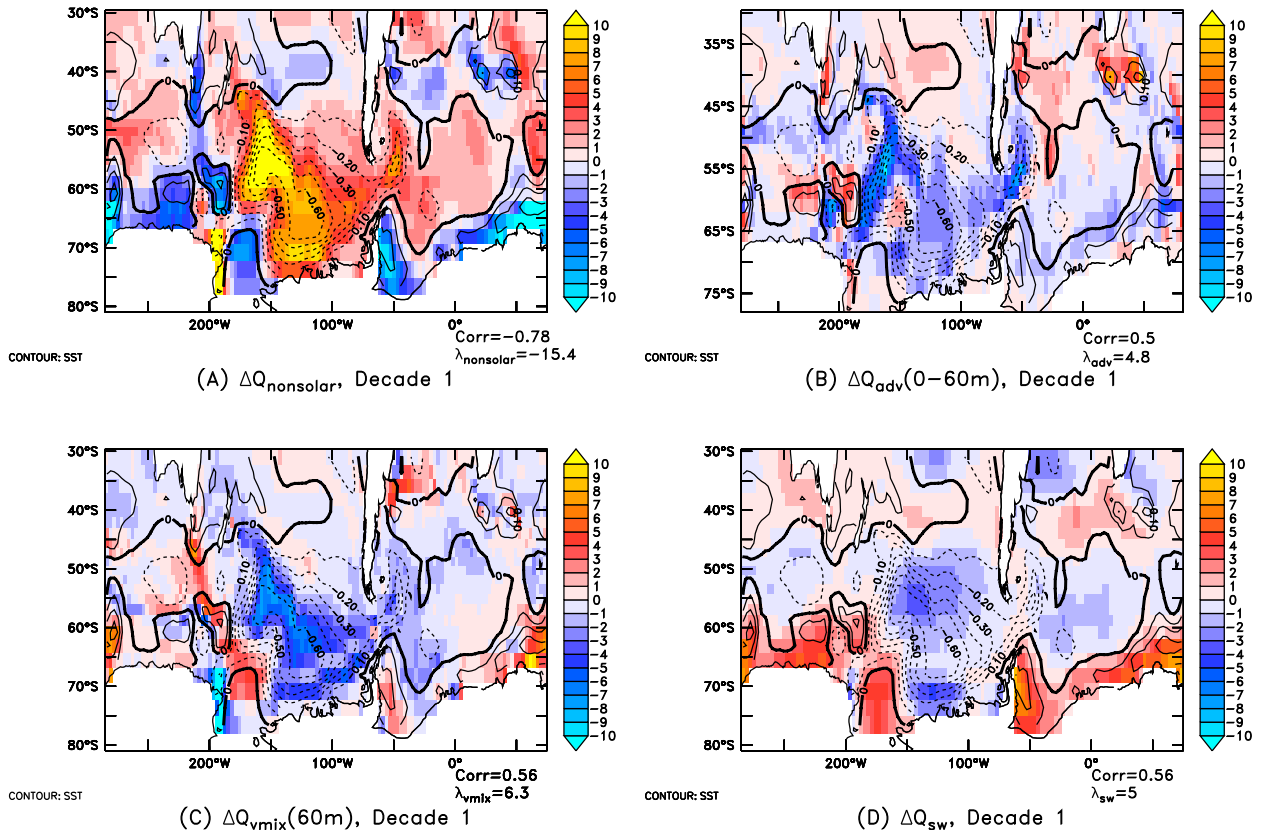


FIG. 4. Relationship between changes in SST (in K; contours) and changes in air–sea (positive into ocean) heat fluxes in W m^{-2} (colors) for the first decade of the ozone perturbation. All results shown from ensemble of 24 simulations. (a) $\Delta Q_{\text{nonsolar}}$ [Eq. (6)] corresponding to the change in fluxes other than net shortwave through the ocean surface. (b) $\Delta Q_{\text{adv}}(0-60\text{ m})$ [Eq. (8a)] corresponding to the net 3D advective heat flux over top 60 m. (c) $\Delta Q_{\text{vmix}}(60\text{ m})$ [Eq. (7a)] corresponding to upward heat flux through 60 m resulting from 1D subgrid-scale mixing processes. (d) ΔQ_{SW} corresponding to the change in shortwave flux into the ocean.

$\Delta Q_{\text{nonsolar}}$ is strongly anticorrelated with the SST anomaly (-0.78) and corresponds to a sensitivity coefficient $\lambda_{\text{nonsolar}} = -15.4 \text{ W m}^{-2} \text{ K}^{-1}$. This is broadly consistent with the observational estimates reported by Armour et al. (2016), who found temperature anomalies of around 0.4 K associated with surface heat flux anomalies of around 6 W m^{-2} . As shown by the black lines in Fig. 5, the anticorrelation between nonsolar heat flux and temperature anomaly stays relatively constant over the course of the experiment, while the associated sensitivity coefficient varies between -15 and $-25 \text{ W m}^{-2} \text{ K}^{-1}$.

Such a large sensitivity coefficient has implications for whether or not one can ignore the time-dependent terms in the heat balance. Analysis of the heat storage over the first decade shows fluxes that are less than 1 W m^{-2} over almost the entire domain, much smaller than $\Delta Q_{\text{nonsolar}}$ and that the associated λ_{tend} varies between -0.2 and $+0.2 \text{ W m}^{-2} \text{ K}^{-1}$ —two orders of magnitude smaller than $\lambda_{\text{nonsolar}}$. One can also look at the importance of time-varying heat content in terms of damping times. For a 60-m-deep mixed layer the heat content associated with

an anomaly of 1 K is only $2.4 \times 10^8 \text{ J m}^{-2} \text{ K}^{-1}$, which the relatively large value of $\lambda_{\text{nonsolar}}$ suggests should decay with a time scale of 120 days. Persistent decadal anomalies on the order of 1 K therefore must therefore be maintained by a relatively strong forcing; that is, there must also be some terms corresponding to the Q in Eq. (7) that have a positive relationship with the temperature anomaly. Given the small values of λ_{tend} , to first order we expect

$$\lambda_{\text{adv}} + \lambda_{\text{vmix}} + \lambda_{\text{SW}} + \lambda_{\text{eddy}} \approx -\lambda_{\text{nonsolar}}. \quad (11)$$

We can then recast the question of how the anomaly is produced in terms of understanding which physical transport terms dominate the larger supply of heat in warm regions and smaller supply of heat in cold regions. F15 point to the importance of advection. They argue that initially horizontal advection of colder water from the south is responsible for cooling the surface throughout the Antarctic, whereas on longer time periods vertical advection of warmer water and its

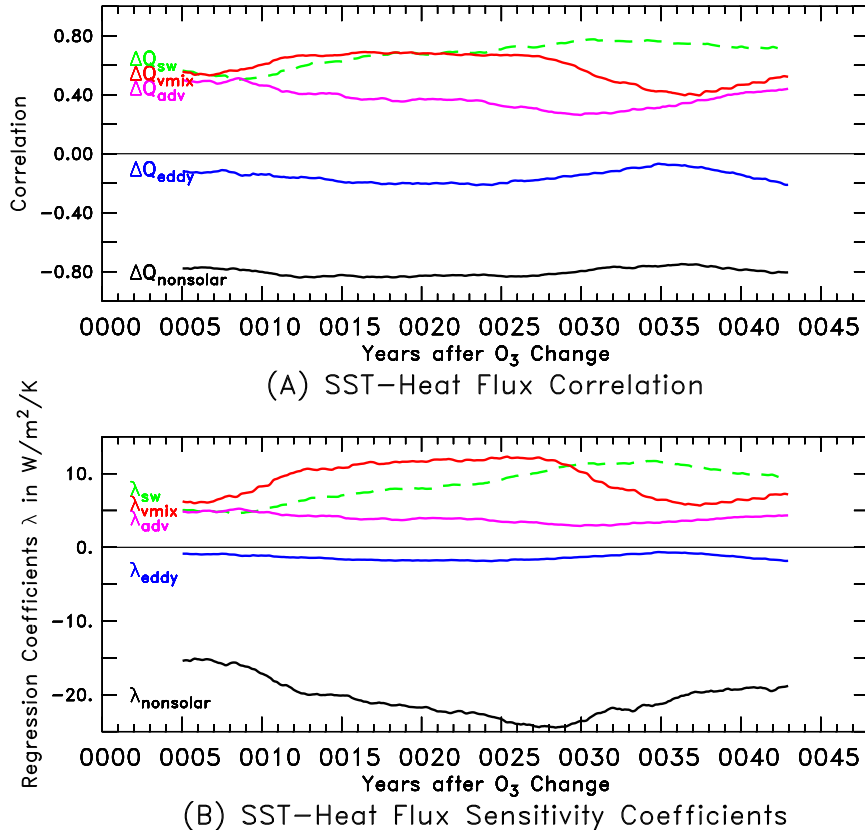


FIG. 5. Relationship between decadal temperature anomaly and heat fluxes over the course of the ozone experiment across the Southern Ocean (80°–30°S) (a) Correlation coefficient. (b) Regression/sensitivity coefficient.

entrainment into the mixed layer bring heat to the surface and cause warming near the continent, which then spreads northward. Given, however, that vertical and horizontal advection are part of one approximately nondivergent velocity field, it is not obvious that they can be separated in cases in which there is a realistic increase in temperature at the base of the mixed layer.

The change in the 3D advective heat tendency over the top 60 m [$\Delta Q_{adv}(0-60\text{ m})$; Eq. (8a)] for the first decade is shown in Fig. 3b. The largest advective cooling is concentrated in the Circumpolar Current region near the date line. Analysis of the changes in horizontal heat transports in this region shows that they do not line up with the changes in Ekman transport, instead showing subtle shifts in the path of the Circumpolar Current and a reduction of the transport of the western boundary current feeding warm water into this region from the north. Although advective heating is positively correlated with the SST anomaly, the correlations over the course of the experiment (magenta line, Fig. 5a) vary between 0.3 and 0.5 and thus explain a relatively small fraction of the variance. The associated sensitivity coefficients [$\lambda_{adv}(0-60\text{ m})$,

magenta line in Fig. 4b] are only 3–4 W m⁻² K⁻¹ and so can balance only about 20% of the changes in nonsolar heat flux. Advection is far from the whole story even during the initial cooling period.

Vertical mixing represents an important additional term. The halocline in the region that is cooling is generally found at a depth of around 60 m. Changes in the vertical diffusive heat flux through this depth [$\Delta Q_{vmix}(60\text{ m})$; Eq. (7a); colors, Fig. 4c] show a pattern that initially helps to explain much of the northern lobe of the Pacific cooling anomaly, with a correlation coefficient of 0.56, somewhat higher than the value for advection, and an initial sensitivity coefficient $\lambda_{vmix} = 6.3\text{ W m}^{-2}\text{ K}^{-1}$. Over the second and third decades both the correlation (red line, Fig. 5a) and regression coefficients (red line, Fig. 5b) rise substantially, so that during this time period changes in the mixing of heat from below are a primary driver of surface heating and/or cooling. Such an important role for the turbulent entrainment in establishing the initial cooling is not part of the picture of F15.

Another difference between our model and MITgcm is the parameterization of clouds, as ESM2Mc accounts

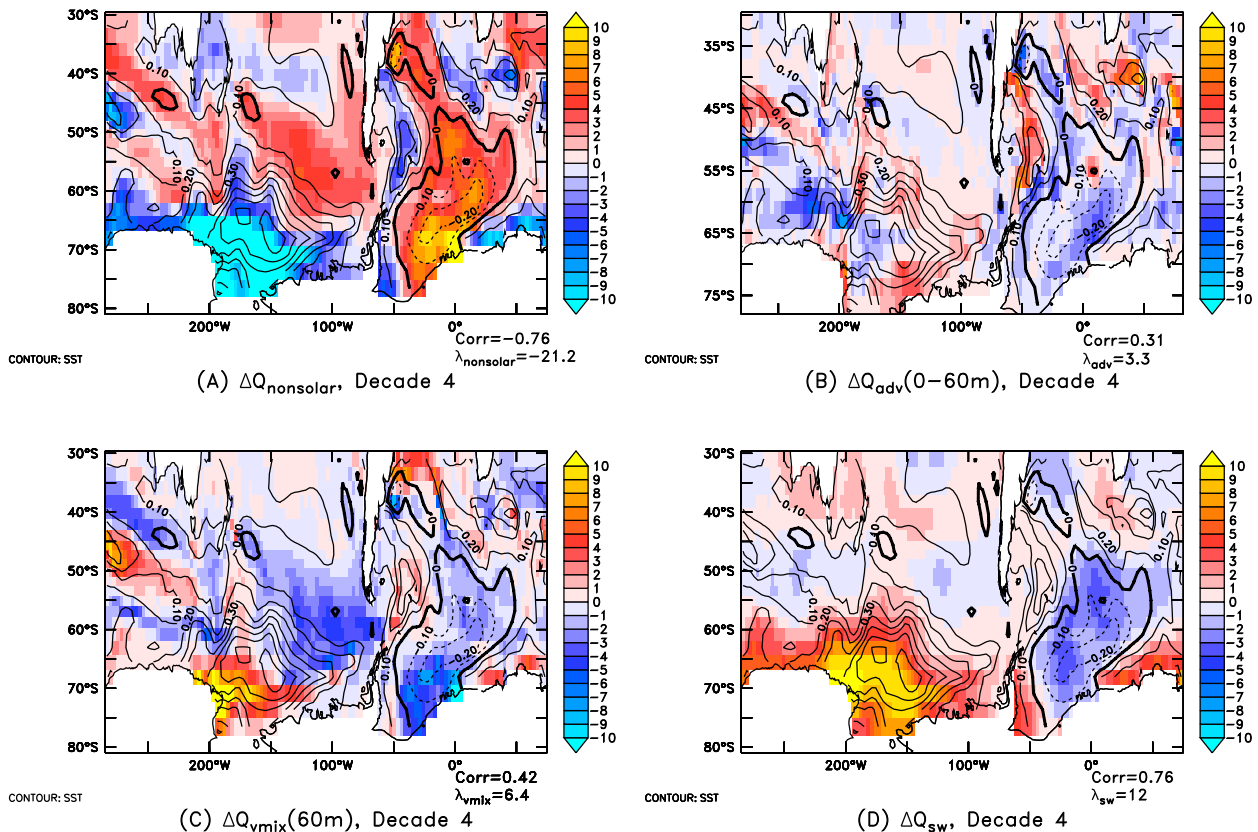


FIG. 6. As in Fig. 3, but for the fourth decade.

for the trade-off between penetrating and large-scale convection. Thus, increasing stability in our model can produce more cloud. The changes in the shortwave flux into the ocean (ΔQ_{SW} , Fig. 4d) also show a strong relationship with the temperature anomalies. In the first decade, the correlation is 0.56 (also somewhat higher than the advective term) with a regression of $5 \text{ W m}^{-2} \text{ K}^{-1}$ so that the role of ΔQ_{SW} in producing the anomalies is initially comparable to the mixing and advective terms. Over time, however, anomalous shortwave absorption replaces vertical diffusion as the primary driver of temperature anomalies, with the correlation coefficient (dashed green line, Fig. 4) rising as high as 0.8 and the sensitivity coefficient exceeding $10 \text{ W m}^{-2} \text{ K}^{-1}$.

If we perform the same analysis as in Fig. 4 on the separate ensembles constructed using the monthly ozone and daily ozone forcing we find patterns that look essentially identical to those in Fig. 4 (and as such are not shown separately). The amplitudes of different fluxes are, however, slightly different and can thus help to explain why these two experiments produce nearly the same response to ozone forcing even though the winds are different. Part of the answer is that Ekman upwelling does not tell the whole story. Although the

advective sensitivity coefficient $\lambda_{adv}(0-60 \text{ m})$ is $4.9 \text{ W m}^{-2} \text{ K}^{-1}$ when daily ozone is used and $4.7 \text{ W m}^{-2} \text{ K}^{-1}$ when monthly ozone is used, the relative difference is far smaller than the $\sim 20\%$ difference in mean wind stress over the latitudes of $70^\circ\text{--}50^\circ\text{S}$. The solar heating acts to reinforce this difference in advection, giving a sensitivity coefficient λ_{SW} of $5.2 \text{ W m}^{-2} \text{ K}^{-1}$ in the daily case, but only $4.8 \text{ W m}^{-2} \text{ K}^{-1}$ in the monthly case. However, other terms act to compensate these changes. The vertical diffusive sensitivity coefficient $\lambda_{vmix}(60 \text{ m})$ is $6.1 \text{ W m}^{-2} \text{ K}^{-1}$ in the daily forcing case and $6.3 \text{ W m}^{-2} \text{ K}^{-1}$ in the monthly forcing case, counteracting the difference in advective forcing. Finally, the sensitivity coefficient associated with nonsolar forcing $\lambda_{nonsolar}$ is $-15.6 \text{ W m}^{-2} \text{ K}^{-1}$ in the daily case, but only $-15.1 \text{ W m}^{-2} \text{ K}^{-1}$ in the monthly case, so that the stronger winds in the daily case may also result in a stronger damping of the temperature anomaly.

It is instructive to contrast the heat flux anomalies during the fourth decade (Fig. 6) with those during the first. The additional shortwave insolation plays an important role in the warming in the western Ross Sea. At the same time, a reduction in shortwave radiation drives additional cooling in the Weddell Sea. These

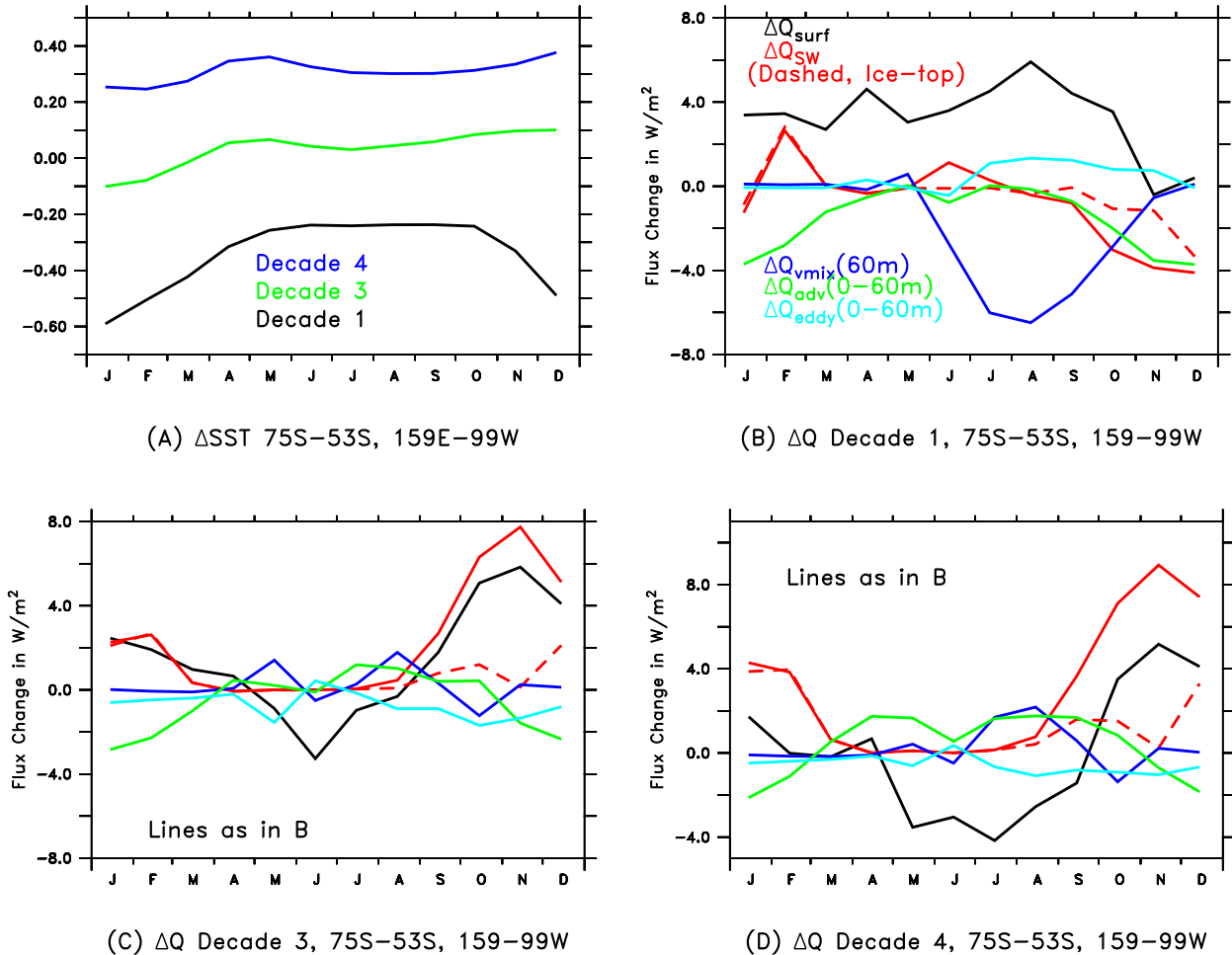


FIG. 7. Seasonal budget of heat fluxes over the top 60 m in initial cold patch in the Pacific sector (75° – 53° S, 159° – 99° W). (a) Seasonal change in temperature (in K) for three separate decades. (b) Monthly changes in heat fluxes in W m^{-2} for the first decade of the perturbation. Black line shows $\Delta Q_{\text{non-solar}}$ [Eq. (6)]. Solid red line shows change in shortwave ΔQ_{SW} defined at ocean surface as in the budget calculations; dashed red line shows this change in defined as the difference in incoming solar radiation at the ice top (indicating changes that are strictly due to clouds). Green line shows $\Delta Q_{\text{adv}}(0-60\text{m})$ [Eq. (8a)]. Light blue line shows $\Delta Q_{\text{eddy}}(0-60\text{m})$ [Eq. (8b)]. Dark blue line shows $\Delta Q_{\text{vmix}}(60\text{m})$ [Eq. (7a)]. (c) As in (b), but for the third decade. (d) As in (b), but for the fourth decade.

opposite-sign changes are reflected in similar changes in total cloudiness (not shown). The sensitivity coefficient for the shortwave heating λ_{SW} is $12 \text{ W m}^{-2} \text{ K}^{-1}$, balancing about half of $\lambda_{\text{non-solar}}$ during this decade. Advection [with $\lambda_{\text{adv}}(0-60\text{m}) = 3.1 \text{ W m}^{-2} \text{ K}^{-1}$] is much less important than vertical mixing [with $\lambda_{\text{vmix}}(60\text{m}) = 6.4 \text{ W m}^{-2} \text{ K}^{-1}$] at this time in the experiment.

c. Flux changes in Pacific sector—Annual cycles

Examination of the annual cycle of heating in the upper mixed layer gives another perspective into how different processes add heat to the mixed layer over time. Figure 7a shows the SST in the Pacific sector over 75° – 53° S, 159° – 99° W. During the first decade the SSTs in this region are cooler throughout the year, with a larger cooling starting

during the austral spring and reaching a maximum during January. During the third decade the temperatures are relatively neutral, whereas during the fourth decade they are relatively warmer.

Analysis of which terms contribute most to this pattern during the first decade shows an important role for $\Delta Q_{\text{adv}}(0-60\text{m})$ (green line, Fig. 7b). The largest change in this term co-occurs with the largest changes in wind stress due to ozone (which occur in late spring) and is thus broadly consistent with the scenario described by F15. Such a seasonal dependence on advection is also consistent with the recent paper of Purich et al. (2016). However, the advection is not the only heat flux that changes. The change in shortwave radiation into the ocean (ΔQ_{SW} ; solid red line) also shows a decrease of the same order of magnitude as the advective term.

Some of this decrease can be traced to a decrease in the amount of shortwave radiation hitting the top of the ice (dashed red line), indicating a reduction in radiation because of cloud feedbacks. The greater part of the decrease in shortwave radiation absorbed by the ocean is not due to clouds, as the decrease in the amount of radiation hitting the ocean (solid red line) is larger than that hitting the top of the ice, indicating an increase in sea ice coverage. Under ozone depletion, as noted in SEA1, sea ice becomes more persistent in the austral spring. The source of this change in sea ice is a reduction in the upward flux of heat due to turbulent mixing through 60 m, (ΔQ_{vdiff} ; dark blue line, Fig. 7b). This flux peaks in the austral winter, when the mixed layer normally entrains warm water from the thermocline. However, the decline in this warming produces little change in sea surface temperatures as the total air–sea flux (ΔQ_{surf} ; black line, Fig. 7b) also shows less net cooling of the ocean.

The annual cycle of fluxes changes significantly if we look at other time periods. During the third decade (Fig. 7c), the annual cycle of the advective flux change $\Delta Q_{\text{adv}}(0 - 60 \text{ m})$ looks similar in pattern but has a smaller magnitude than in the first decade. However, the surface heat fluxes are significantly different, particularly the shortwave flux change ΔQ_{SW} , which is positive during the austral spring. During the fourth decade (Fig. 7d) we see that while the annual cycle $\Delta Q_{\text{adv}}(0 - 60 \text{ m})$ (lower in the summer, higher in the winter) is similar to that in previous decades, the mean value is quite different. This means that advection warms the top 60 m during the wintertime but slightly cools it in the summer. The wintertime advective warming is balanced by more surface heat loss. The summertime advective cooling is overwhelmed by additional shortwave absorption, driven by less ice from October through December and less cloudiness (red dashed and solid lines overlap) in January and February. In the third and fourth decades, changes in the mixing of heat from below (blue lines, Figs. 7c,d) are relatively small.

d. Salinity changes as a driver of variability

How is the variability in the mixing of heat from below driven? On the face of things, it would appear that wintertime cooling should be associated with more mixing. However, much of the Antarctic is unstably stratified with respect to temperature; it is salinity that controls the stratification. During the winter, warm surface waters from the upper thermocline may be entrained into the mixed layer, ameliorating surface cooling. The rate at which this occurs is governed by a bulk Richardson number Ri_b :

$$\text{Ri}_b = \frac{g\Delta\rho H}{\rho u_t^2}, \quad (12)$$

where $\Delta\rho$ is the density difference across the base of the mixed layer, H is the mixed layer depth, and u_t is a turbulent velocity. This bulk Richardson number is extremely sensitive to changes in stratification. For a mixed layer that is 60 m deep and a critical Ri of $O(1)$, a salinity difference between the mixed layer and upper thermocline of 0.01 PSU corresponds to a relatively large turbulent velocity of 0.07 m s^{-1} . Small changes in the stratification can thus seriously limit penetration of turbulence from the mixed layer into the upper thermocline. This can be seen in Fig. 8a, which shows the evolution of $\Delta Q_{\text{nonlocalKPP}}(60 \text{ m})$ averaged over $159^\circ - 99^\circ \text{W}$ as a function of latitude and time. Annual mean declines in the upward heat flux of up to 5 W m^{-2} are seen between latitudes 50° and 70°S and years 0 and 30. Focusing on a point at 55°S , 140°W during the winter months of July–September only (Fig. 8b), we see that increasing salinity stratification results in remarkably large decreases in upward fluxes of up to 24 W m^{-2} during these months with both the timing and vertical extent of changes in upward heat fluxes tightly linked to changes in the magnitude of stratification. Note that this change in convection is very different from the deep convection occurring in the Weddell Sea, which penetrates to much greater depths.

What drives these changes in salinity stratification? As shown in Fig. 9, sea surface salinities over the first 10 years of the perturbation run decrease in exactly the same region where temperature (Figs. 3a and 4) and vertical mixing of heat from below (Fig. 4b) decrease. Linking salinity changes to the spatial pattern of forcing is more complicated than for temperature, as one does not expect atmospheric fluxes to damp anomalies. While the Southern Ocean as a whole sees an increase in precipitation over this time period (Fig. 9b), precipitation appears to decrease in much of the region where the salinity decreases. However, evaporation (Fig. 9c) decreases over the cooler region, which reinforces the negative salinity anomaly (which in turn feeds back on the cooling). The net surface water flux (Fig. 9d) shows a freshening over most of the Southern Ocean with very large increases in water flux along the southern edge of the cooling region linked to more net melting of sea ice. Integrating over the entire Southern Ocean south of 52°S (Fig. 10) the tendency of the surface layers to lose salt (black line) is primarily driven by this additional freshwater flux (dark blue line) with advection and vertical diffusion working against the stronger vertical gradients to make the surface layer saltier. Interestingly, the impact of changing subgrid-scale eddy fluxes (magenta line) is to enhance the salt anomaly at the surface, although whether this is due to changes in eddy-induced

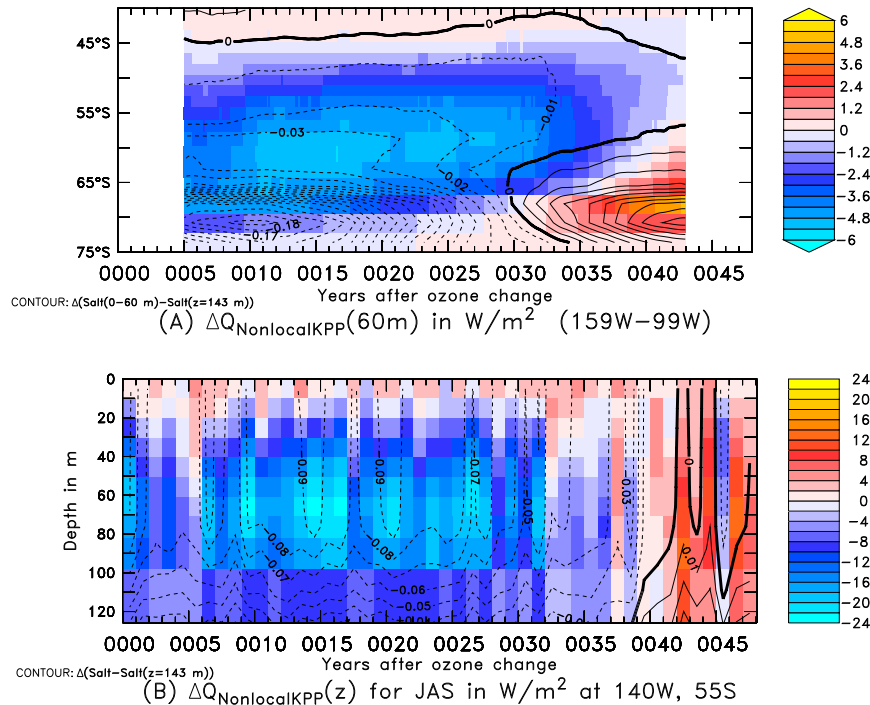


FIG. 8. Changes in the KPP nonlocal heat flux and its relationship with the strength of the halocline over the course of the experiment. (a) Decadally smoothed $\Delta Q_{\text{nonlocalKPP}}(60\text{m})$ in W m^{-2} at 60 m averaged between 159° and 99°W as a function of time and latitude. Contours of changes in the halocline strength (salinity averaged over the top 60 m minus that at 143 m) overlaid. (b) $\Delta Q_{\text{nonlocalKPP}}(z)$ at 55°S , 140°W with change in salinity relative to 143 m overlaid.

stirring along isopycnals or eddy-induced advection is not currently clear. After about 25 years, the vertical mixing is able to break through the stratification, reversing the salinity tendency and switching the system to a more convective state. The resulting warming increases evaporation, reducing the freshening tendency from surface fluxes. Advective salt transport into the mixed layer increases during this time period, making the system more unstable to vertical mixing, while eddy fluxes change to remove more salt from the mixed layer, stabilizing the surface. There is some suggestion toward the end of the time period that the system is on its way to switching back toward a less convective state.

4. Conclusions

Both here and in *SEA1*, we have demonstrated that a fully coupled model of the Earth system with realistic parameterizations for complex atmospheric processes is capable of producing a decadal-scale cooling of the Southern Ocean in response to an ozone hole. This suggests that the difference between the long-term cooling found in the idealized MITgcm versus the short-term cooling found in the more comprehensive CCSM3.5 reflects details of CCSM3.5 and is not an

intrinsic property of including realistic geometry and more complex parameterizations of atmospheric convection. A careful analysis of the term balances behind the change shows that the primary mechanism proposed by *F15* for explaining the initial cooling (namely Ekman advection) is only part of the story. The full set of feedbacks is schematically illustrated in *Fig. 11*. In addition to causing a shift in the winds, the ozone hole is also associated with changes in precipitation and clouds. The southward shift of winds over the Southern Ocean does in fact cause an advective cooling, particularly as it shifts the balance of waters entering the Circumpolar Current near New Zealand (*Fig. 4a*). However, the southward shift of precipitation associated with the shift of the winds acts to freshen the Southern Ocean as a whole (*Fig. 10*) and changes in the cycling of sea ice produce more ice melt in the southeast Pacific. The resulting freshening of the southeast Pacific acts to cut off the upward mixing of heat from below the mixed layer (*Figs. 4b, 5, and 8*), driving a much more widespread cooling. The cooling acts to reduce evaporation (*Fig. 9c*), producing a positive feedback on salinity, mixing, and temperature. Radiative feedbacks also play a major role in establishing the spatial pattern of temperature change (*Fig. 5*), with changes in sea ice

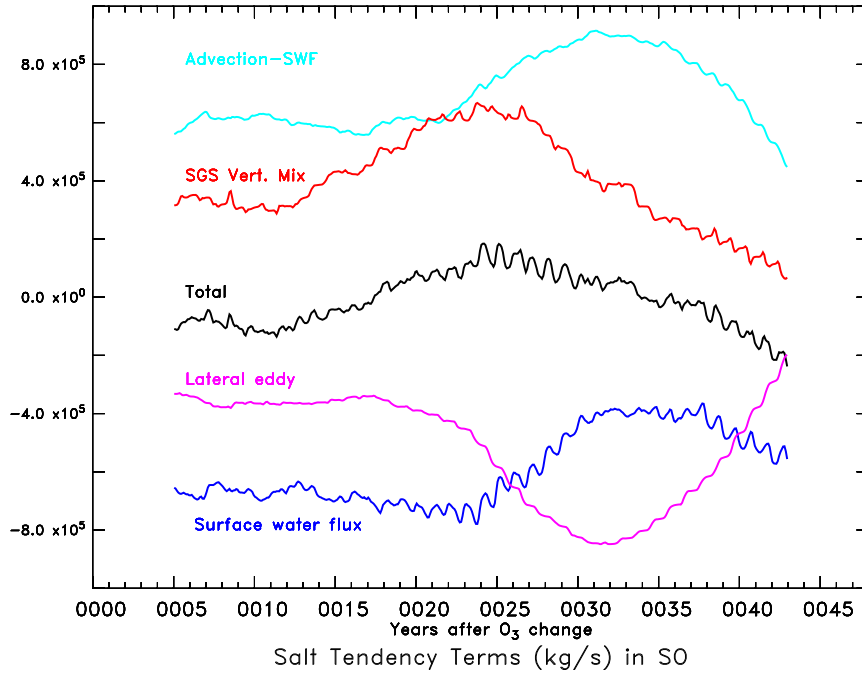


FIG. 10. Salt balance terms relative to the control integrated over the Southern Ocean south of 52°S.

region became about 0.1 PSU fresher at the surface, a value quite consistent with the ESM2Mc ozone perturbation runs. However, when averages are taken over the whole Antarctic (not shown) the model shows no change increase in the vertical gradient, while the observations show changes very similar to those in Fig. 12d. This suggests that ozone-induced changes in salinity stratification could play a role in modulating changes in the salinity over the entire Southern Ocean, which may be driven by global warming and the concomitant increase of the hydrological cycle (Durack and Wijffels 2010).

The complex picture presented in Fig. 11 suggests a number of possible reasons for the differences between

the CCSM3.5 and GFDL models. The first is in the details of eddy mixing. CCSM3.5 has a very high Gent–McWilliams mixing coefficient in the surface layers, which should tend to suppress convection, and indeed de Lavergne et al. (2014) find that the CESM model (a lineal descendant of CCSM3.5) is one of the least convective CMIP5 models. Insofar as it is the feedback between the salinity and upward mixing of heat that is primarily responsible for cooling in our model, the absence of this feedback in CESM may explain why it does not have a strong cooling response. Attention thus needs to be paid to the interaction between horizontal and vertical mixing [as noted by Gnanadesikan et al. (2007)]. Recent work done

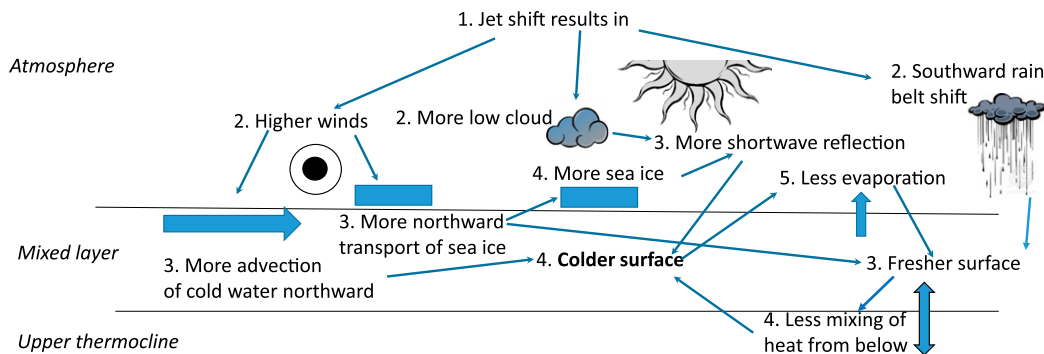


FIG. 11. Flow diagram of forcings and feedbacks involved in establishment of initial cooling. Diagram looks westward. All processes are assumed to be occurring in approximately the same region (nominally from about 70° to 50°S), so that processes farther to the right should not be thought of as displaced northward.

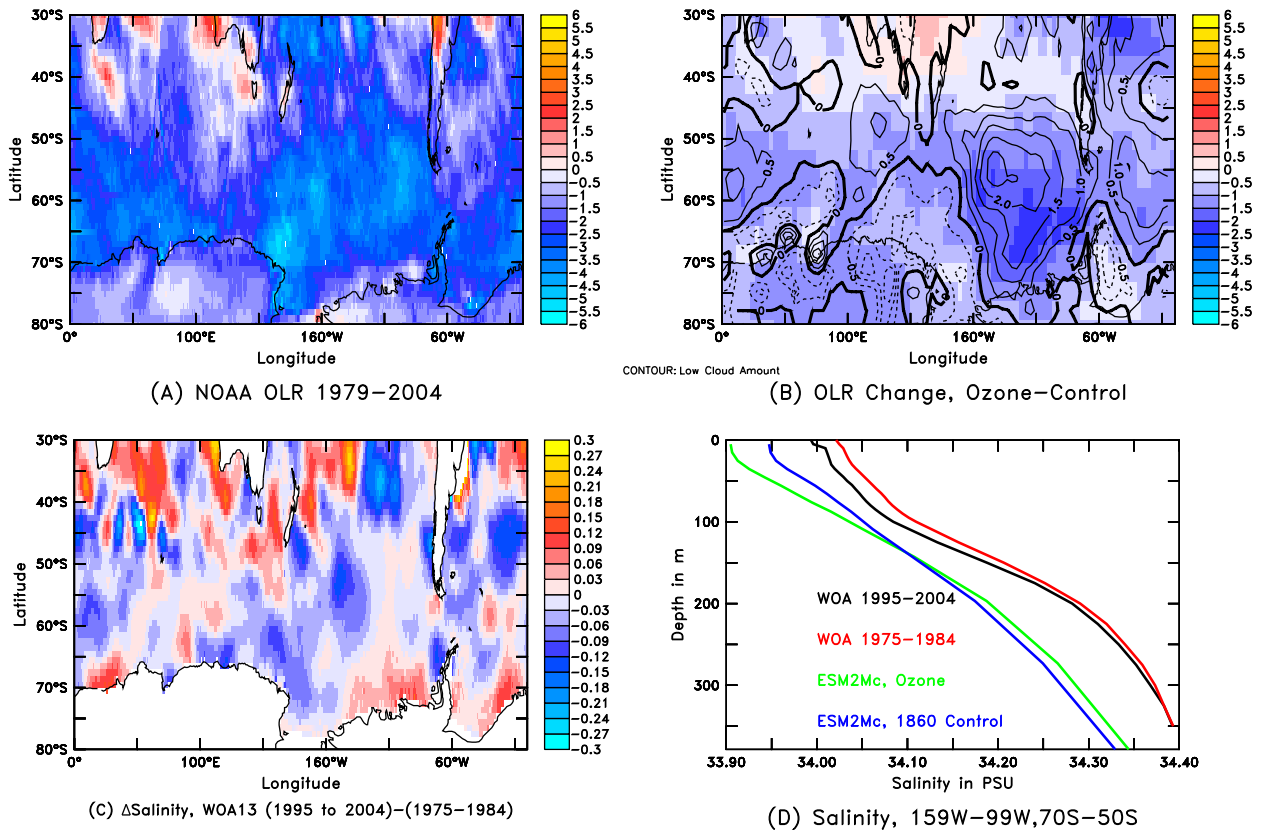


FIG. 12. Comparison of observed changes with the changes caused in the model by ozone. (a) Outgoing longwave radiation (OLR) trend from 1979–2004 using the dataset of Lee (2014). (b) Difference in OLR between ozone perturbation and control simulations of ESM2Mc. (c) Change in salinity in the *World Ocean Atlas 2013* (WOA13) dataset of Zweng et al. (2014) between the decade centered on 1999 minus the decade centered on 1979. (d) Comparison of the salinity profiles for 1995–2004 (black) and 1975–84 (red) in WOA13 and the perturbed ozone ensemble run (green) and control (blue) from ESM2Mc averaged over the same longitude band as in Fig. 8, focusing on the region of maximum cooling in the model.

in our group suggests that Weddell Sea deep convection can be turned off in ESM2Mc by changing the minimum coefficient associated with the Gent–McWilliams parameterization. We plan to repeat the ozone hole forcing within that model configuration in the near future.

A second difference between the CCSM3.5 and ESM2Mc models is the location of the wind stress perturbation associated with the ozone hole. CCSM3.5 places this perturbation far to the south of where both the observations and ESM2Mc place it. As a result, the perturbation wind-driven circulation in CCSM3.5 is largely contained within a region with permanent sea ice. As it mixes heat up from below CCSM3.5 may thus see a much larger sea ice albedo feedback than ESM2Mc (and likely than in the real world).

Finally, the GFDL, MITgcm, and NCAR families of models differ in how they parameterize clouds, which affects the interaction between clouds and changes in the Southern Hemisphere jet and how rapidly stratus and shallow cumulus clouds increase as surface waters

cool. Grise and Polvani (2014) showed that the jet–cloud feedback differed substantially among CMIP5 models, with another lineal descendant of CCSM3.5 (CCSM4) being one of those models where a southward shift of the jet tended to produce fewer clouds and the GFDL models being in the class where a southward shift of the jet produced more cloud. In MITgcm, by contrast, cloud feedbacks play a relatively minor role in the response to ozone (F15), which may also contribute to a longer initial cooling. Given that Grise and Polvani (2014) suggest that the response seen in CCSM4 is not supported by observations, this would suggest that the longer-term cooling is more realistic. Trossmann et al. (2016) also find that the magnitude of the shift in the location of the atmospheric jet (and thus presumably the rain belt as well) is tightly linked to cloud feedbacks rather than to changes in the ocean temperature, suggesting that such feedbacks may vary from model to model. However, it should be noted that the GFDL models tend to have too little cloud over the summertime Southern Ocean,

leading to excessive summertime warming (Delworth et al. 2006) despite having relatively realistic sea ice during the winter (Pradal and Gnanadesikan 2014). This bias, which is common in CMIP3 models (Trenberth and Fasullo 2010), may reflect too strong a coupling between sea surface temperature changes and clouds, which would suggest that the GFDL response may be too strong. Alternatively, however, it may simply mean that this feedback is triggered by other biases in the model, such as potentially excessively strong mixing that destabilizes the halocline (Pradal and Gnanadesikan 2014).

Acknowledgments. This work was supported by the National Science Foundation under NSF proposal FESD-1338814. We thank David Trossman, Jordan Thomas, David Ferreira, and four anonymous reviewers for useful comments on an earlier version of the manuscript. Interpolated OLR data provided by NOAA/OAR/ESRL PSD, Boulder, CO, United States, from their web site (<http://www.esrl.noaa.gov/psd>).

REFERENCES

- Armour, K., J. Marshall, J. R. Scott, A. Donohoe, and E. R. Newsom, 2016: Southern Ocean warming delayed by circumpolar upwelling and equatorward transport. *Nat. Geosci.*, **9**, 549–554, doi:10.1038/ngeo2731.
- Bitz, C., and L. Polvani, 2012: Antarctic climate response to stratospheric ozone depletion in a fine resolution climate model. *Geophys. Res. Lett.*, **39**, L20705, doi:10.1029/2012GL053393.
- Branstator, G., 1985: Analysis of general circulation model sea-surface temperature anomaly simulations using a linear model. Part I: Forced solutions. *J. Atmos. Sci.*, **42**, 2225–2241, doi:10.1175/1520-0469(1985)042<2225:AOGCMS>2.0.CO;2.
- Cionni, I., and Coauthors, 2011: Ozone database in support of CMIP5 simulations: Results and corresponding radiative forcing. *Atmos. Chem. Phys.*, **11**, 11 267–11 292, doi:10.5194/323acp-11-11267-2011.
- Dee, D. P., and Coauthors, 2011: The ERA-Interim reanalysis: Configuration and performance of the data assimilation system. *Quart. J. Roy. Meteor. Soc.*, **137**, 553–597, doi:10.1002/qj.828.
- de Lavergne, C., J. B. Palter, E. D. Galbraith, R. Bernardello, and I. Marinov, 2014: Cessation of deep convection in the open Southern Ocean under anthropogenic climate change. *Nat. Climate Change*, **4**, 278–282, doi:10.1038/nclimate2132.
- Delworth, T., and Coauthors, 2006: GFDL's CM2 global coupled climate models. Part I: Formulation and simulation characteristics. *J. Climate*, **19**, 643–674, doi:10.1175/JCLI3629.1.
- Durack, P. J., and S. E. Wijffels, 2010: Fifty-year trends in global ocean salinity and their relationship to broad-scale warming. *J. Climate*, **23**, 4342–4362, doi:10.1175/2010JCLI3377.1.
- Ferreira, D., J. Marshall, C. M. Bitz, S. Solomon, and A. Plumb, 2015: Antarctic Ocean and sea ice response to ozone depletion: A two-time-scale problem. *J. Climate*, **28**, 1206–1226, doi:10.1175/JCLI-D-14-00313.1.
- Fox-Kemper, B., and Coauthors, 2011: Parameterization of mixed layer eddies. III: Implementation and impact in global ocean climate simulations. *Ocean Modell.*, **39**, 61–78, doi:10.1016/j.ocemod.2010.09.002.
- Galbraith, E. D., and Coauthors, 2011: The impact of climate variability on the distribution of radiocarbon in CM2Mc—A new Earth system model. *J. Climate*, **24**, 4230–4254, doi:10.1175/2011JCLI3919.1.
- Gent, P., and J. C. McWilliams, 1990: Isopycnal mixing in ocean models. *J. Phys. Oceanogr.*, **20**, 150–155, doi:10.1175/1520-0485(1990)020<0150:IMIOCM>2.0.CO;2.
- Gille, S. T., 1997: The Southern Ocean momentum balance: Evidence for topographic effects from numerical model output and altimeter data. *J. Phys. Oceanogr.*, **27**, 2219–2232, doi:10.1175/1520-0485(1997)027<2219:TOSOMBE>2.0.CO;2.
- Gnanadesikan, A., S. M. Griffies, and B. L. Samuels, 2007: Effects in a climate model of slope tapering in neutral physics schemes. *Ocean Modell.*, **16**, 1–16, doi:10.1016/j.ocemod.2006.06.004.
- , M.-A. Pradal, and R. Abernathy, 2015: Isopycnal mixing by mesoscale eddies significantly impacts oceanic anthropogenic carbon uptake. *Geophys. Res. Lett.*, **42**, 4249–4255, doi:10.1002/2015GL064100.
- Griffies, S. M., A. Gnanadesikan, R. C. Pacanowski, V. D. Larichev, J. K. Dukowicz, and R. D. Smith, 1998: Isoneutral diffusion in a z-coordinate ocean model. *J. Phys. Oceanogr.*, **28**, 805–830, doi:10.1175/1520-0485(1998)028<0805:IDIAZC>2.0.CO;2.
- Grise, K., and L. M. Polvani, 2014: Southern Hemisphere cloud-dynamics biases in CMIP5 models and their implications for climate projections. *J. Climate*, **27**, 6074–6092, doi:10.1175/JCLI-D-14-00113.1.
- Hallberg, R. W., and A. Gnanadesikan, 2001: An exploration of the role of transient eddies in determining the transport of a zonally re-entrant current. *J. Phys. Oceanogr.*, **31**, 3312–3330, doi:10.1175/1520-0485(2001)031<3312:AEOTRO>2.0.CO;2.
- Large, W. G., J. C. McWilliams, and S. C. Doney, 1994: Oceanic vertical mixing: A review and a model with a nonlocal boundary layer mixing parameterization. *Rev. Geophys.*, **32**, 363–403, doi:10.1029/94RG01872.
- Latif, M., T. Martin, and W. Park, 2013: Southern Ocean sector centennial climate variability and recent decadal trends. *J. Climate*, **26**, 7767–7782, doi:10.1175/JCLI-D-12-00281.1.
- Lee, H.-T., 2014: Climate Algorithm Theoretical Basis Document (C-ATBD): Outgoing longwave radiation (OLR)—Daily. NOAA Climate Data Record (CDR) Program, CDR-ATBD-0526, 46 pp.
- Marshall, J., J. Scott, K. C. Armour, J.-M. Campin, M. Kelley, and A. Romanou, 2015: The ocean's role in the transient response of climate to abrupt greenhouse gas forcing. *Climate Dyn.*, **44**, 2287–2299, doi:10.1007/s00382-014-2308-0.
- Martin, T., W. Park, and M. Latif, 2013: Multi-centennial variability controlled by Southern Ocean convection in the Kiel Climate Model. *Climate Dyn.*, **40**, 2005–2022, doi:10.1007/s00382-012-1586-7.
- Menemenlis, D., I. Fukumori, and T. Lee, 2005: Using Green's functions to calibrate an ocean general circulation model. *Mon. Wea. Rev.*, **133**, 1224–1240, doi:10.1175/MWR2912.1.
- Parkinson, C. and N. E. diGirolamo, 2016: New visualizations highlight new information on the contrasting Arctic and Antarctic sea ice trends since the 1970s. *Remote Sens. Environ.*, **183**, 198–204, doi:10.1016/j.rse.2016.05.020.
- Pradal, M. A. and A. Gnanadesikan, 2014: How does the Redi parameter for mesoscale mixing impact climate in an Earth system model? *J. Adv. Model. Earth Syst.*, **6**, 586–601, doi:10.1002/2013MS000273.
- Purich, A., W. Caj, M. H. England, and T. Cowan, 2016: Evidence for link between modelled trends in Antarctic sea ice and

- underestimated westerly wind changes. *Nat. Commun.*, **7**, 10409, doi:10.1038/ncomms10409.
- Ramaswamy, V., and Coauthors, 2001: Radiative forcing of climate change. *Climate Change 2001: The Scientific Basis*, J. T. Houghton et al., Eds., Cambridge University Press, 349–416.
- Russell, A. M., and A. Gnanadesikan, 2014: Understanding long-period variability in ENSO amplitude. *J. Climate*, **27**, 4037–4051, doi:10.1175/JCLI-D-13-00147.1.
- Seviour, W., A. Gnanadesikan, and D. W. Waugh, 2016: The transient response of the Southern Ocean to stratospheric ozone depletion. *J. Climate*, **29**, 7383–7396, doi:10.1175/JCLI-D-16-0198.1.
- Simmonds, I., 2015: Comparing and contrasting the behavior of Arctic and Antarctic sea ice over the 35 year period 1979–2013. *Ann. Glaciol.*, **56**, 18–28, doi:10.3189/2015AOG69A909.
- Thomas, J., D. W. Waugh, and A. Gnanadesikan, 2015: Southern Hemisphere extratropical variability: Recent trends and natural variability. *Geophys. Res. Lett.*, **42**, 5508–5515, doi:10.1002/2015GL064521.
- Trenberth, K. E., and J. T. Fasullo, 2010: Simulation of present-day and twenty-first-century energy budgets of the southern oceans. *J. Climate*, **23**, 440–454, doi:10.1175/2009JCLI3152.1.
- Troen, I. B., and L. Mahrt, 1986: A simple model of the atmospheric boundary layer; sensitivity to surface evaporation. *Bound.-Layer Meteor.*, **37**, 129–148, doi:10.1007/BF00122760.
- Trossman, D. S., J. B. Palter, T. M. Merlis, Y. Huang, and Y. Xia, 2016: Large-scale ocean circulation–cloud interactions reduce the pace of transient climate change. *Geophys. Res. Lett.*, **43**, 3935–3943, doi:10.1002/2016GL067931.
- Turner, J., T. J. Bracegirdle, T. Phillips, G. J. Marshall, and J. S. Hosking, 2013: An initial assessment of Antarctic sea ice extent in the CMIP5 models. *J. Climate*, **26**, 1473–1484, doi:10.1175/JCLI-D-12-00068.1.
- , J. S. Hosking, G. J. Marshall, T. Phillips, and T. J. Bracegirdle, 2016: Antarctic sea ice increase consistent with variability of the Amundsen Sea low. *Climate Dyn.*, **46**, 2391–2401, doi:10.1007/s00382-015-2708-9.
- Zweng, M. M., and Coauthors, 2014: *Salinity*. Vol. 2, *World Ocean Atlas 2013*, NOAA Atlas NESDIS 74, 39 pp.